# Experimental validation of the buckling behavior of unreinforced and reinforced composite conical-cylindrical shells for launch-vehicles

Tillotson Rudd, Michelle; Schultz, Marc R.; Gardner, Nathaniel W.; Kosztowny, Cyrus J.R.; Bisagni, Chiara

**DOI**
10.1016/j.compstruct.2024.118493

**Publication date**
2024

**Document Version**
Final published version

**Published in**
Composite Structures

**Citation (APA)**
Tillotson Rudd, M., Schultz, M. R., Gardner, N. W., Kosztowny, C. J. R., & Bisagni, C. (2024). Experimental validation of the buckling behavior of unreinforced and reinforced composite conical-cylindrical shells for launch-vehicles. *Composite Structures*, *349-350*, Article 118493. https://doi.org/10.1016/j.compstruct.2024.118493

Composite Structures 349–350 (2024) 118493

Contents lists available at ScienceDirect

Composite Structures

journal homepage: www.elsevier.com/locate/compstruct

# Experimental validation of the buckling behavior of unreinforced and reinforced composite conical-cylindrical shells for launch-vehicles

Michelle Tillotson Rudd [a], Marc R. Schultz [b], Nathaniel W. Gardner [b], Cyrus J.R. Kosztowny [b], Chiara Bisagni [c,d,*]

[a] NASA Marshall Space Flight Center, Huntsville, AL, USA
[b] NASA Langley Research Center, Hampton, VA, USA
[c] Politecnico di Milano, Milan, Italy
[d] Delft University of Technology, Delft, the Netherlands

ARTICLE INFO

*Keywords:*
Buckling
Composites
Conical-cylindrical
Testing
Nonlinear analysis
Imperfections

ABSTRACT

Conical-cylindrical shells are common geometries in launch-vehicle structures as stage adapters and payload adapters, and they are susceptible to buckling due to their large radius-to-thickness ratios. Buckling design guidance is available but it is limited for conical and cylindrical shells. There is no available buckling design guidance for conical-cylindrical shells. This paper presents the validation of two finite element models used to successfully predict the buckling behavior of a composite conical-cylindrical shell with and without reinforcement tested in two separate campaigns. The laminate design for the first test campaign consisted of a quasi-isotropic layup. For the second test campaign, additional composite plies were applied to reinforce the transition region of the original laminate. The work presented demonstrates the ability to predict the buckling behavior of a composite conical-cylindrical shells with two different designs, which may aid in creating buckling design guidance for conical-cylindrical shells. Additionally, this paper shows that there is no appreciable benefit to adding reinforcement to the transition region if the intent is to increase the buckling load, due to the fact reinforcement brings increased buckling imperfection sensitivity to the shell.

## 1. Introduction

Launch vehicles are comprised of conical and cylindrical shell sections. The cylindrical shape is a main component of launch vehicles due to its high strength-to-volume ratio. Conical sections are utilized when transitioning from different-diameter cylindrical components such as the transition between first and second stages. Conical structures are also employed for payload adapters, which are nested within the launch vehicle. Currently, there are a number of different launch-vehicle structures that combine the conical and cylindrical shells with a smooth toroidal transition region to create a unitized conical-cylindrical shell. An example of a conical-cylindrical structure is the NASA Space Launch System (SLS) Universal Stage Adapter (USA) [1] that is being proposed for a future SLS configuration. Other examples include the Système de Lancement Double Ariane (Sylda) on the Ariane 5, and the Vega Secondary Payload Adapter [2]. Buckling is one of the possible failure modes for launch-vehicle structures and consequently is an important consideration in design. Though conical-cylindrical shells are currently being used in the aerospace industry, there is no buckling design guidance like there is for separate conical or cylindrical shell components. NASA published empirically based buckling knockdown factors (KDF) in NASA SP-8007 [3] and NASA SP- 8019 [4] for cylindrical and conical shells, respectively, that may be used in the design process, but it is largely accepted that these empirical KDFs are overly conservative.

The empirically based KDFs are used to account for differences between test and analysis, which are largely attributable to radial imperfections and can be specific to the structural design. The buckling capability of a shell is related of the imperfection sensitivity, meaning the greater the imperfection sensitivity the lower the design buckling load. Researchers have investigated how to design imperfection insensitive shell structures with the goal to increase the design buckling load. One way to design imperfection insensitive shell structures was by stabilizing the postbuckling response to prevent a large loss in load after an initial buckling event. Bisagni and Cordisco [5] manufactured and tested stiffened composite cylinders to assess the performance in the

* Corresponding author at: Politecnico di Milano, Milan, Italy.
*E-mail address:* chiara.bisagni@polimi.it (C. Bisagni).

https://doi.org/10.1016/j.compstruct.2024.118493
Received 20 June 2024; Received in revised form 6 August 2024; Accepted 16 August 2024
Available online 17 August 2024

postbuckling range. Ning and Pellegrino took a nontraditional approach by investigating cylinders with wavy cross sections to demonstrate imperfection insensitive designs [6,7]. Lincoln, et al. took an alternative approach by designing imperfection insensitive composite cylinders with variable tow angles. Using variable tow angles breaks up the symmetry in the prebuckling strain field, which may reduce the cylinder's sensitivity to imperfections [8]. Wagner, et al. used machine learning to optimize buckling load and imperfection insensitivity [9]. Additionally, it was demonstrated by Rudd, et al. that conical-cylindrical shells can be designed to be insensitive to radial imperfections, which may save mass [10].

In addition to radial imperfections, tow overlaps and gaps due to the automated fiber placement (AFP) manufacturing constraints have been demonstrated to affect the buckling behavior of small-scale composite test articles. For example, Rudd, et al., [11] determined that the probable reason for the discrepancy between the test data and numerical predictions of the buckling of a composite conical-cylindrical shell was due to the assumption made when incorporating the unavoidable tow overlaps into the finite element model. The concept of design for manufacturing can be used to account for potential tow gaps, overlaps, and other manufacturing constraints during the AFP process. To account for these new manufacturing-based details in the design, the build of the part can be simulated, and the overlaps and gaps can be estimated. Then a process to modify the design to minimize the gaps and overlaps can be completed [12,13].

Specifically, regarding the buckling behavior of composite conical-cylindrical shells, the minimal research publicly available to this shape is primarily specific to the piping and civil industry [14,15]. With regard to aerospace applications, Chronopoulos, et al. focused on the dynamic response of a composite conical-cylindrical-conical shell in which the geometry was based on the Sylda [16]. More recently Rudd, et al. published research on the buckling of composite conical-cylindrical shells and how current design practices compare [10]. Their research showed that the currently used empirically based KDF approach may not be appropriate for conical-cylindrical shells. Rudd, et al. published test and analysis correlation of a composite conical-cylindrical shell, referred to as 3CHELL [11], with the intent of demonstrating the ability to predict the buckling behavior of a conical-cylindrical shell and providing data toward the development of buckling design guidelines.

In order to develop buckling design guidance, more than one test of a conical-cylindrical shell with an associated finite element model (FEM) to successfully predict the buckling behavior will be required. Meanwhile, the test and analysis results of a second buckling test of a composite conical-cylindrical shell was completed. The first buckling test article, 3CHELL, buckled elastically after the first test campaign. The test article was undamaged, and additional composite reinforcement was added to the transition region. The modified test article with reinforcement will be referred to herein as Re3CHELL.

The use of FEM to predict the buckling behavior of a composite conical-cylindrical shell without and with reinforcement, 3CHELL and Re3CHELL, respectively, will be demonstrated. The design and manufacturing details of 3CHELL and Re3CHELL are discussed in Section 2. Next, the finite element model of 3CHELL and Re3CHELL is discussed in Section 3. This includes information pertaining to an updated 3CHELL FEM based on manufacturing data, and how the manufacturing data influenced the FEM of Re3CHELL. The experimental setup for Re3CHELL is included in Section 4. The updated 3CHELL FEM is compared to the 3CHELL experimental data in Section 5.1, and the Re3CHELL FEM is compared to the Re3CHELL experimental data in Section 5.2. The effect of adding reinforcement to a composite conical-cylindrical shell by comparing the buckling response of 3CHELL and Re3CHELL is discussed in Section 5.3. Concluding remarks are presented in Section 6.

## 2. Description of test articles

A composite conical-cylindrical shell test article referred to as 3CHELL was built and tested by loading in axial compression until buckling. It was determined after a visual inspection and brief analysis of the data that there was no permanent deformation or material failure. Therefore, the buckling test was repeated. During the second test, the test article buckled within 1 % of the first buckling test and buckling initiated in the same location [11].

Following the completion of the test, 3CHELL was brought back to the manufacturing lab and inspected using thermography, a nondestructive evaluation technique. No damage was detected, which provides additional evidence that the buckling events were elastic. The seemingly elastic buckling response provided a unique opportunity to modify 3CHELL. It had previously been demonstrated numerically that the transition area between the conical and cylindrical portions of a conical-cylindrical shell was critical to the buckling behavior [10]. Therefore, it was decided to add reinforcement to the transition region of 3CHELL and repeat the buckling test. The test article 3CHELL with added reinforcement to the transition region is referred to as Re3CHELL.

The original shell, 3CHELL, had a quasi-isotropic laminate of $[45/-45/90/0]_S$ and was fabricated with Hexcel IM7/8552–1* (190 gsm) preimpregnated carbon fiber epoxy tows that were 6.35 mm wide. The test article was built on an aluminum mandrel at NASA Marshall Space Flight Center using an AFP robot. The measured ply thickness was 0.171 mm, and the material properties for IM78552-1 were taken from data published by the National Institute for Aviation Research [17] and are presented in Table 1. The test-article geometry is an approximate scaled-down version of the SLS USA. The overall dimensions are presented in Fig. 1a. The test article was centered in aluminum end rings and held in place with a ring of epoxy potting compound on the outer mold line (OML) and the inner mold line (IML). The end rings were machined from an aluminum plate with an assumed modulus of elasticity of 71.01 GPa and Poisson's ratio of 0.33 [18]. The epoxy potting compound had an assumed modulus of elasticity of 7.58 GPa with a Poisson's ratio of 0.33 [19].

Two layers of Toray plain-weave fabric T1100G 3960 PW [20] were adhered to the IML surface of 3CHELL in the region indicated by the box in Fig. 1a using an autoclave cure process. The fabric plies were placed so that the 0-degree orientation aligned with the axis of rotation of the test article. The reinforcing fabric was placed on the IML because the test article OML surface had been painted for digital image correlation (DIC), which was used to collect displacement and strain data during the test of 3CHELL. The design details for the reinforcement are shown in Fig. 1b, where the acreage region is the original 3CHELL layup, and ply1 and ply 2 consisted of the plain-weave fabric. The fabric was approximately 0.20-mm thick. Ply 2 covered ply 1 with a 6.35 mm overlap on the top and bottom. Not pictured is a layer of film adhesive FM 209–1 [21] which was 0.25 mm in thickness that was placed between the acreage and the added fabric plies. The transition region had a compound curvature so each ply and film adhesive was cut into 8 sections to reduce the amount of wrinkling. The seams for fabric ply 1, fabric ply 2, and the film adhesive were staggered. A picture of the cured reinforcement plies as viewed axially upwards is shown in Fig. 2. The moduli for the fabric is presented in Table 1 [20]. The Poisson's ratio was estimated to be 0.05 based on references [22–24].

The shape of test article Re3CHELL was measured in the same manner as 3CHELL, using the structured light scanning photogrammetry method after the cure of the additional reinforcement plies to determine

**Table 1**
Nominal material properties.

| Material | $E_{xx}$ (GPa) | $E_{yy}$ (GPa) | $G_{xy}$ (GPa) | $\nu_{xy}$ (−) |
|---|---|---|---|---|
| IM7/8552–1 | 140.9 | 9.72 | 4.69 | 0.356 |
| T1100G 3960 PW | 77.9 | 86.9 | 5.1 | 0.05 |

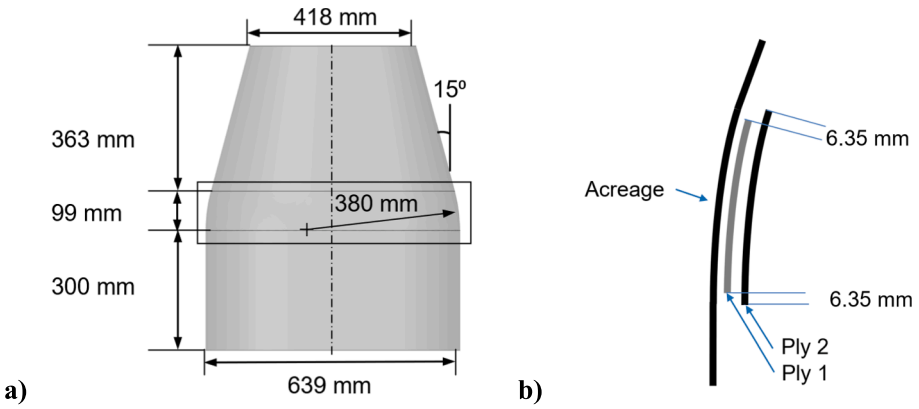


**Fig. 1.** Re3CHELL (a) dimensions and location of reinforcement, and (b) reinforcement detail.

**Fig. 2.** Close up image of the reinforcement after cure.

the IML and OML radial imperfections and thickness variations. The IML and OML radial imperfections are presented in Fig. 3a where the cooler colors represent relatively inward imperfection, and the warmer colors represent a relatively outward imperfection. The overall peak-to-peak amplitude of the radial imperfection was approximately 1.50 mm, which was slightly larger than the overall thickness of the laminate at 1.37 mm.

The measured thickness is shown in Fig. 3b, and the red band at the transition region corresponds to the added thickness from the reinforcing fabric plies. Red hatched lines, corresponding to an increased thickness region, were observed in the conical region of the shell. These lines relate to the overlapped areas of the ± 45-degree plies. Each course of composite unidirectional tape was laid from the cylindrical end to the conical end. In the cylindrical region of the shell, one course contained four tows of unidirectional tape. To ensure no gapping occurred between tows while transitioning from the cylinder to the tapered conical end, adjacent courses overlapped by a full tow width of 6.35 mm. The overlapped area increased from the bottom towards the conical end until the red lines abruptly end near the top of the cone. At this location, the tow of the currently laid course has overlapped an entire tow width of the adjacent course that was previously laid, and the overlapping composite tow was dropped. The course continues up the length of the conical region with three tows remaining.

## 3. Numerical analysis using updated 3CHELL FEM and Re3CHELL FEM

The original 3CHELL finite element model was created in Abaqus 2021 [25]. The FEM consisted of the four-node, reduced integration shell element, S4R, with approximately 3.8 mm side lengths to model the laminate, potting compound, and end rings. The ± 45-degree overlapped areas were modeled discretely by plotting the curve for a constant fiber angle along the length of a conical section, Fig. 4a. From this, the surface of the conical shell could be divided into different regions so the nominal layup, referred to as acreage lay, and the overlapped areas could be defined separately. A detailed view of the overlapped areas can be seen in Fig. 4b. The mesh size was largely determined by the size of an element required to account for the overlapped areas. For example, the location of where the tow was dropped, and width of the tow was known. The overlapped area reduced monotonically until the transition region. To account for the tapered area, the FEM for the original 3CHELL model was divided into four regions and section properties were assigned based on observations and using the measured 3CHELL weight as a guide. The first region, near the cone top, contained only the acreage layup depicted by the cyan color in Fig. 4a. The second region contained

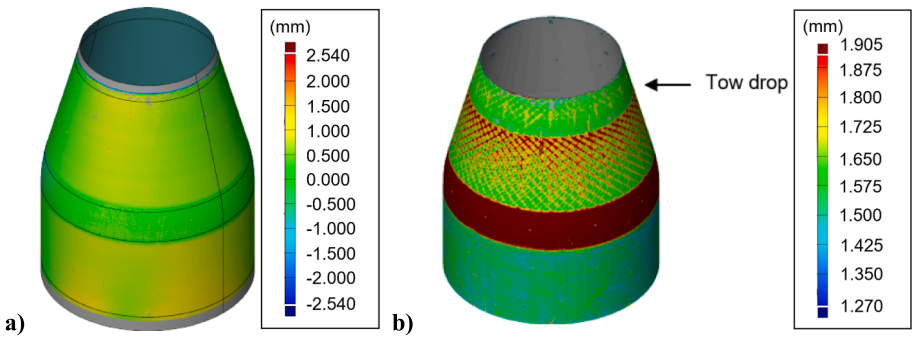


**Fig. 3.** Structured light scan data of Re3CHELL: (a) radial imperfections of IML; (b) measured thickness.

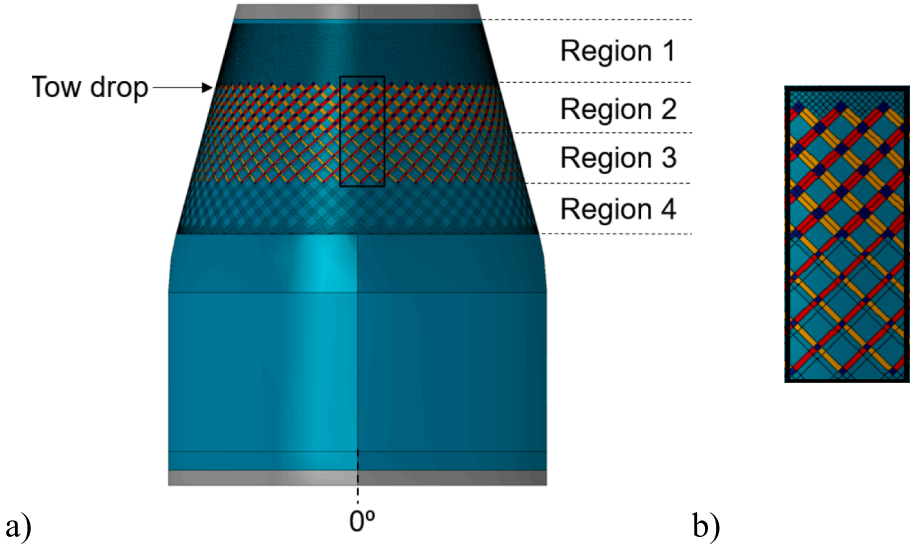


**Fig. 4.** Original 3CHELL FEM with highlighted section properties (a) and detailed view of overlap sections (b).

an overlap width equal to one tow width. The overlapped areas for the + 45-degree plies are represented by red, and the – 45 degree overlapped areas are represented by yellow. Where the + and – 45-degree plies overlap is represented by dark blue. The next region assumed an overlapped width equal to half of a tow width, the red and yellow areas are half the width than those in the second section. The last region, just above the transition region, contained no overlapped areas. The section property definitions are reported in Table 2. More details pertaining to the finite element model for the original 3CHELL can be referenced in [11].

A FEM of Re3CHELL was created by modifying the original 3CHELL FEM to account for the additional fabric plies. Both FEMs consisted of the four-node, reduced-integration shell element, S4R, with the same element size. Additionally, geometric nonlinear analyses were completed to determine the buckling load for both models. The geometric nonlinear analysis was completed using the dynamic implicit solver, in which the axial displacement rate was 0.076 mm/min. The measured IML radial imperfections were also included. From the original test and analysis correlation of 3CHELL, it was determined that the discrepancy between the test data and the FEM was largely due to assumptions made when incorporating the ± 45-degree plies tow overlaps.

It was not until after the test of Re3CHELL that it was learned that the program used to control the AFP robot, Vericut Composite Programming (VCP) [26] provided by CGTech[1], can be used to estimate parameters such as the tow overlaps per ply. Comparing the VCP output to the original FEM, the VCP estimate of overlapped areas from the ± 45-degree tows was approximately 28 % greater than what was assumed in the original 3CHELL FEM. Additionally, the original model assumed that there were no regions with overlapping 0-degree tows, however the VCP estimated an area associated with the 0-degree-tows.

Once VCP was used to estimate the overlaps, the original 3CHELL FEM was updated to reflect the larger predicted overlapped area. This new FEM will be referred to as the updated 3CHELL model. To account for the additional ± 45-degree overlaps, more elements in the FEM were assigned the section properties inclusive of the +45 and −45 overlaps. The pattern of the overlapped tows was similar to the original 3CHELL FEM, but the yellow and red areas corresponding to the overlapped + 45-degree and –45-degree plies, respectively, extend all the way to the top of the transition. The updated 3CHELL FEM with newly defined section properties is shown in Fig. 5 and listed in Table 4. Additionally, a new section was defined to account for the overlapped 0-degree is shown in magenta. Since the 0-degree overlapped areas are concentrated towards the conical end due to the shrinking diameter, the region above the tow drop (Region 1 from Fig. 4) was modified. The 0-degree overlapped area specified by VCP was 16 % of the magenta region. To account for the increase in overlapped area, the thickness of the 0-degree plies was increased by 16 % from the as-measured thickness of 0.171 mm to 0.185 mm. These modifications increased the 3CHELL FEM weight from 3.31 kg to 3.34 kg, which was closer to the measured weight of 3.40 kg. The area of the overlapped regions, as determined by the VCP program, are compared in Table 3 with what was assumed in developing the original 3CHELL model and the updated 3CHELL model.

The main difference between the updated 3CHELL FEM and the Re3CHELL FEM was the inclusion of the reinforced regions shown in black and white in Fig. 5b. The white region has film adhesive and two plain weave fabric plies on the IML. The black region has the film adhesive and only one fabric ply. For all FEMs, the positive global X-axis of the FEM aligns with the 0-degree circumferential location of the test article, the positive global Y-axis aligns with the 90-degree circumferential location of the test article, and global Z axis is defined along the axis of rotation. In all models, the measured IML radial imperfections were incorporated into the FEM because the OML data was highly influenced by the thickness variations that were primarily due to the tow overlaps.

The updated 3CHELL FEM and the Re3CHELL FEM contained two reference points on the top and bottom of the test article centered along the axis of rotation. Tie constraints were used to connect all degrees of freedom to the respective reference points. The top reference point had all rotational degrees of freedom fixed. The primary source of loading was due to an applied axial displacement (Z), but it was observed that the load platen applied a shearing displacement in the X-Y plane during the test of 3CHELL. Therefore, the X and Y translational degrees of freedom (X and Y) were not fixed to account for the measured shearing displacement. The bottom reference point had all degrees of freedom fixed. A geometrically nonlinear implicit dynamic analysis was used to predict the buckling response of 3CHELL and Re3CHELL.

**Table 2**
Section properties of the original 3CHELL.

| Section | FEM color | Stacking Sequence |
|---|---|---|
| Acreage | Cyan | 45/-45/90/0/0/90/-45/45 |
| +45 overlap | Red | 45/**45**/-45/90/0/0/90/-45/**45**/45 |
| −45 overlap | Yellow | 45/-45/-**45**/90/0/0/90/-**45**/-45/45 |
| +45 and −45 overlap | Dark blue | 45/**45**/-45/-**45**/90/0/0/90/-**45**/-45/**45**/45 |
| Potted ends | Gray | Al ring/Potting/Acreage/Potting/Al ring |

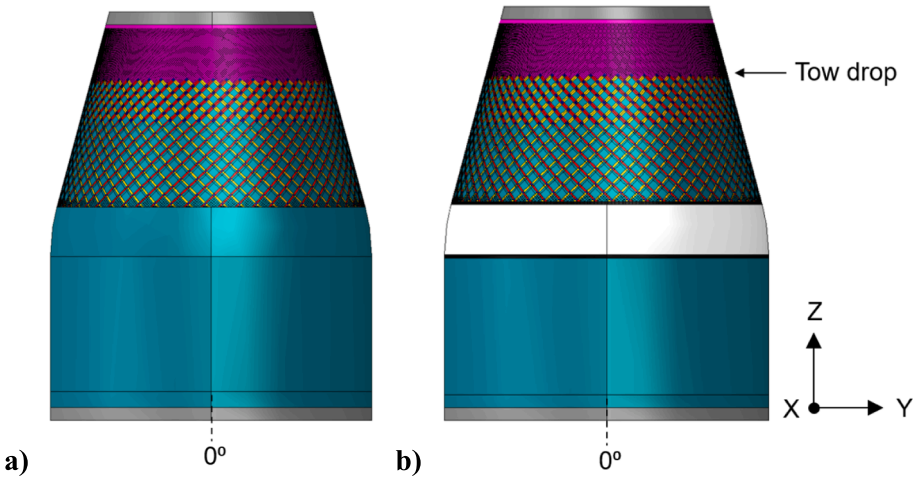


**Fig. 5.** Finite element models: (a) updated 3CHELL; (b) Re3CHELL.

**Table 3**
Tow overlap areas from VCP and finite element models.

| Ply | VCP | Original 3CHELL FEM | Updated3CHELL FEM |
|---|---|---|---|
| ± 45-degree overlaps | 0.39 $m^2$ | 0.28 $m^2$ | 0.40 $m^2$ |
| 0-degree overlaps | 0.03 $m^2$ | 0.00 $m^2$ | 0.03 $m^2$ |

**Table 4**
Added section properties of the updated 3CHELL and Re3CHELL FEMs.

| Section | FEM color | Stacking Sequence |
|---|---|---|
| Acreage w/modified 0-ply | Magenta | 45/-45/90/0/0/90/-45/45 |
| Padup- 2 plies | White | 45/-45/90/0/0/90/-45/45/Film adhesive/ T1100/ T1100 |
| Padup- 1 ply | Black | 45/-45/90/0/0/90/-45/45/Film adhesive/ T1100/ |
| Potted ends | Gray | Al ring/Potting/Acreage/Potting/Al ring |

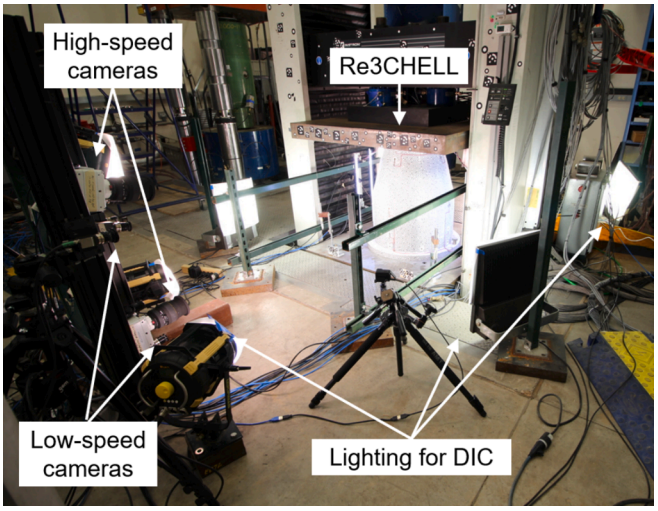


**Fig. 6.** Experimental setup of Re3CHELL.

## 4. Experimental setup

The experimental setup and instrumentation for 3CHELL and Re3CHELL were identical. The test article was instrumented and was subjected to several subcritical load sequences prior to the final load sequence to failure. Instrumentation included strain gages, and low-speed and high-speed DIC systems were used to monitor the test article prebuckling, buckling, and postbuckling response throughout all load sequences. The experimental set up of Re3CHELL is shown in Fig. 6.

The test article was covered with a high-contrast speckle pattern for DIC to accommodate two different fields of view (global and local). The global field of view was used for the low-speed and high-speed cameras centered at the 0-degree and 180-degree circumferential locations and encompassed the entire length of the test article including the end rings, approximately 711 mm x 864 mm. The cameras used to capture the entire test article and interface rings will be referred to as the global systems. A smaller, more localized field of view was defined with additional low-speed cameras positioned at the 0, 90, 180, and 270-degree circumferential locations. The local field of view encompassed a smaller area, approximately 297 mm x 365 mm, and focused on the transition region. Due to the fact that the local camera systems had smaller fields of view, higher spatial resolutions (pixel/mm) could be obtained without interfering with the data being collected by the global camera systems. The local field of view was chosen because it was anticipated there would be high strain gradients in this region due to the curvature and ply drops from the added reinforcement. A more detailed description of the test setup can be found in reference [11].

## 5. Results and discussion

The test and analyses correlation for the test article 3CHELL using the updated 3CHELL finite element model based on manufacturing data output from the VCP program is discussed in this section. Next, the results for Re3CHELL are presented in Section 5.2. Finally, the buckling behavior of 3CHELL and Re3CHELL are compared in Section 5.3.

### 5.1. Updated 3CHELL results

A comparison of the load versus displacement data up to and including the buckling limit point of the updated 3CHELL FEM and the test data is presented in Fig. 7. The test article 3CHELL buckled at a load of 251.8 kN [11]. The updated 3CHELL model with included measured radial imperfections and the X-Y-plane shearing displacement from the load frame had a predicted buckling load of 247.2 kN, which was within 2 % of the measured buckling load. The inclusion of radial imperfections reduced the predicted buckling load by 5 %. While, the predicted and measured buckling loads were similar, the predicted and measured stiffness are not well aligned. However, it was suggested in Ref 11 that

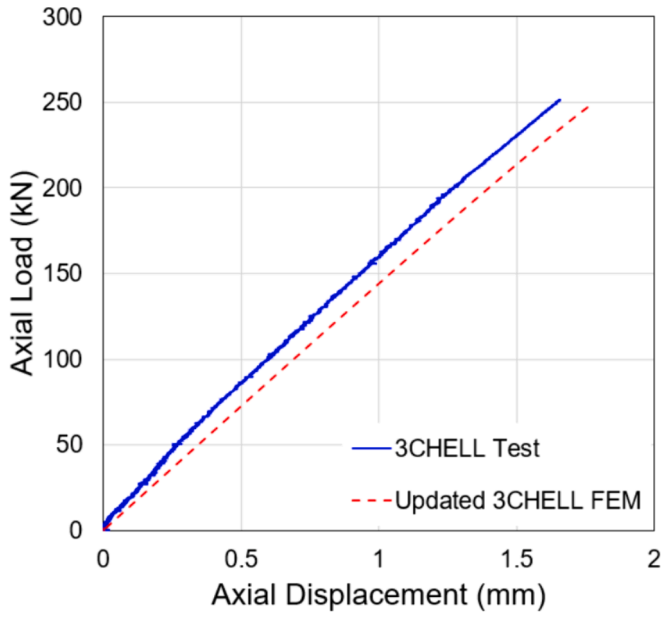


**Fig. 7.** Axial load versus axial displacement curves from test and updated 3CHELL FEM.

the difference between the FEM stiffness and the measured stiffness was potentially attributable to a gap between 3CHELL and the bottom surface of the end ring. The presences of such a gap could not be verified because the end rings were never removed, so no additional effort was made to determine the source of stiffness change. The updated 3CHELL model predicted buckling to initiate in the cylinder just below the transition region at the 0-degree circumferential region as shown in the predicted radial displacement plots, Fig. 8. The cooler colors (e.g., blues and blacks) represent relatively inward displacement, and the warmer colors (e.g., reds and orange) represent relatively outward deformation. During the testing of 3CHELL, buckling also initiated in the cylinder just below the transition region, but at approximately the 125-degree circumferential location (circled) instead, as shown in the radial displacement plots in Fig. 9.

### *5.2. Re3CHELL results*

The test article Re3CHELL buckled at a load of 268.7 kN and its postbuckled configuration is shown in Fig. 10. The load versus displacement curves up to and including the buckling limit point from the test data and the Re3CHELL FEM are presented in Fig. 11. Re3CHELL was predicted to buckle at 304.5 kN without measured radial imperfections (dashed black curve), and 275.5 kN with IML measured radial imperfections (dashed green curve). The inclusions of measured radial imperfections led to a reduction in the buckling load of 9.5 %. This reduction was greater than the predicted decrease in load-carrying capability due to imperfections for 3CHELL, which was only 5 %. As in 3CHELL, the load frame caused the top load platen to move perpendicular to the test article axis of rotation in the X-Y plane. This resulted in a shearing displacement measured at the top of the test article. This shearing displacement had a magnitude of 0.28 mm towards the 34-degree circumferential location. This shearing displacement and the radial imperfections resulted in a predicted buckling load of 275.2 kN (red curve), which was within 2.5 % of the tested load (blue curve).

It was confirmed with high-speed DIC that buckling occurred approximately at the 125-degree circumferential location at an axial position just above the tow drop in the conical region. The progression of the experimental buckling event is shown in Fig. 12a–f using a sequence of data from the high-speed DIC system centered at the 0-degree circumferential location. In Fig. 12, the warmer colors represent relative outward displacement, and the cooler colors represent relatively inward displacement. In Fig. 12a buckling initiation is observed in the upper left-hand corner of the image near the conical end, where the edge of a purple dimple can be observed (circled). Approximately 0.5 ms after that shown in Fig. 12a, a secondary dimple forms adjacent to the first (Fig. 12b). Then, 2.0 ms after the first image, buckling has propagated with a series of buckling waves around the entire top circumference of the conical section (Fig. 12c). Fig. 12d was taken 5.5 ms after the first image and shows a second row of dimples forming just below the first. In Fig. 12e, the newly formed row of dimples has become larger, while the first row become smaller. Eventually, postbuckling equilibrium was reached in the final image (Fig. 12f), which is consistent with Fig. 10.

The predicted and measured radial displacements (U1) at incipient buckling for Re3CHELL are shown in Figs. 13 and 14, respectively, with the buckling location circled. Buckling was predicted to occur in the conical region above the tow drop just outside of the DIC field of view at approximately the 90-degree location, which is shown in Fig. 13c for clarity. This was similar to the location that buckling was observed to initiate in Re3CHELL as determined using the high-speed DIC data. Buckling initiated just out of the field of view of the high-speed cameras, and it was therefore difficult to confirm the exact location. Similar patterns can be observed in the predicted and measured radial displacements, most notably the inward deformations in the blue just above the tow drop in the conical section and the maximum outward displacement at the transition region. The measured maximum outward displacement was 0.63 mm, as measured by the DIC system centered about 0-degree circumferential location (Fig. 14a). For the same field of view centered about 0-degrees in the FEM (Fig. 13a), the predicted maximum outward displacement was 0.60 mm. The minimum inward displacement occurs just above the tow drop. The measured inward deformation was 0.38 mm, as observed in the DIC system centered about

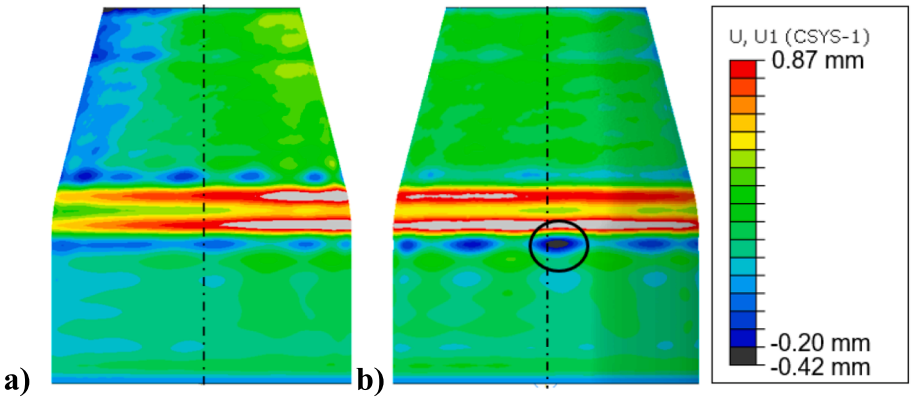


**Fig. 8.** Predicted radial displacements (U1) from updated 3CHELL FEM: (a) centered at 0 degrees; (b) centered at 180 degrees.

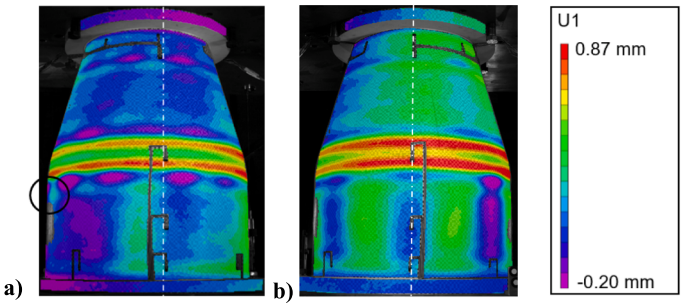


**Fig. 9.** Measured radial displacements (U1) of 3CHELL: (a) centered at 0 degrees; (b) centered at 180 degrees.

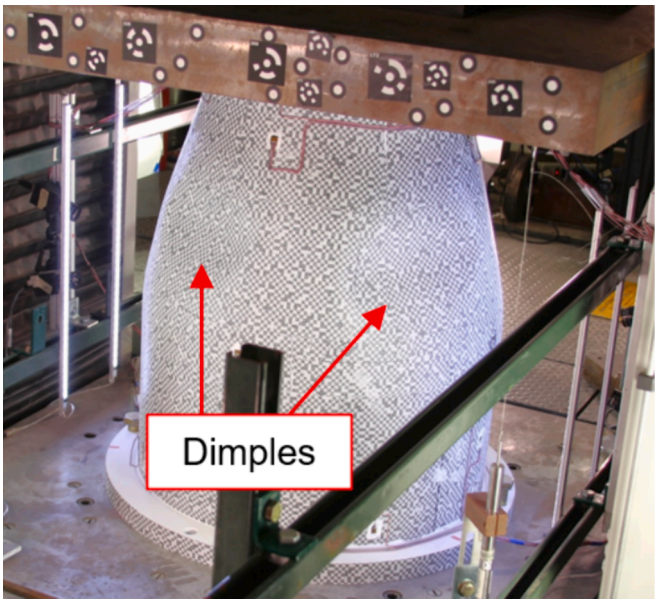


**Fig. 10.** Postbuckled configuration of Re3CHELL.

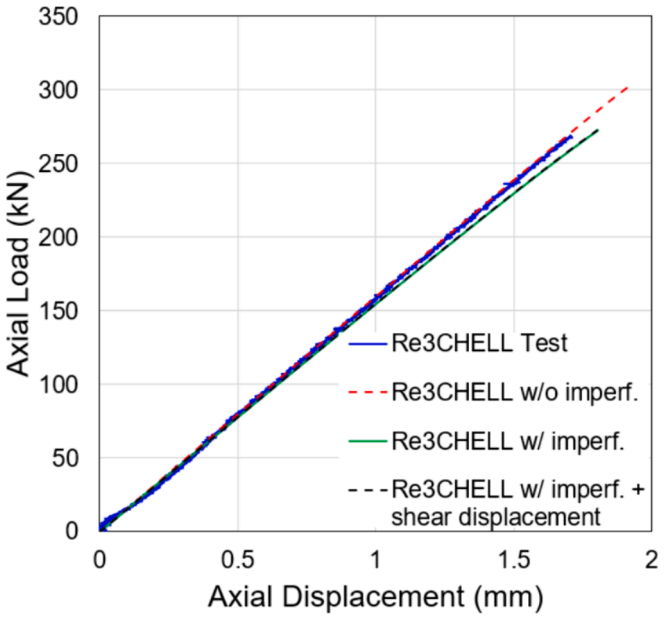


**Fig. 11.** Axial load versus axial displacement curves from test and Re3CHELL FEM.

180 degrees (Fig. 14b). In the same field of view for the FEM (Fig. 13b), the predicted inward displacement was 0.19 mm. The predicted inward displacement was half of the measured inward displacement; however, both occur in a dimple in the tow drop region. One difference that can be observed occurs where the reinforcement ply 1 was terminated just above and below the transition region. In the FEM, there was a sharp gradient of outward radial displacement (red bands) where the reinforcement ply ends. This is not observed in the measured radial displacements.

The predicted and measured minimum principal (primarily in the axial direction for the current work) strains at incipient buckling are presented in Figs. 15, 16, 17. There was a red band of low minimum principal strain at the transition region in both predicted and measured results. Also, at the conical end there was a band of green which corresponds to a higher axial strain. The greatest predicted minimum principal strain was −5749 με, which was about 60 % higher than the greatest measured minimum principal strain of −3560 με. The stiffness discontinuities due to the tow drops in the FEM led to an artificially high strain in the predicted results, which may be a contributing factor as to why the difference between the measured and predicted minimum principal strains was observed.

The spatial resolution of the local DIC systems was 3.5-times higher than the global system, meaning there were more pixels per millimeter in the field of view. This means that the local systems could accurately capture areas with high strain gradients, such as the tow drop region and the transition region. The field of view of the local systems did not include the tow drop region, but it did include the transition region. The area boxed in Fig. 15b and Fig. 16b corresponds to the field of view of the local DIC system centered at 180 degrees. The high strain gradients predicted are presented as thin circumferential bands that extend outward from the transition region red to green to gray (Fig. 15) and are not visible in the data from the global DIC systems (Fig. 16). Although, the high strain gradients can also be observed in the results from the local DIC systems in Fig. 17. The image on the left in Fig. 17 is the area in the black box in Fig. 15, and the image on the right is the local view of the test article. Two strain gages, SG1 and SG2, can be observed in the local view of the test article. Two areas are highlighted in Fig. 17 that correspond to high stress gradients in the FEM that were measured by the local DIC systems, but not the global systems.

As mentioned previously when reporting the values of minimal principal strain, the discrepancy between the measured and predicted values was most likely due to the stiffness discontinuities in the FEM. It was demonstrated that using the local DIC systems with the higher spatial resolution could more accurately measure high strain gradients, which can improve correlation when directly comparing the measured DIC data to the predicted FEM.

Evaluating the strain gage data can also provide valuable information on the correlation between test and analysis. The strain data presented is for the gages SG1 and SG2 and appear in the local system field of view in Fig. 17. The calculated axial membrane strain data from the OML and IML strain gages in the transition region (SG1) and cylinder at 180 degrees (SG2) is presented in Fig. 18. There was only a 3 %

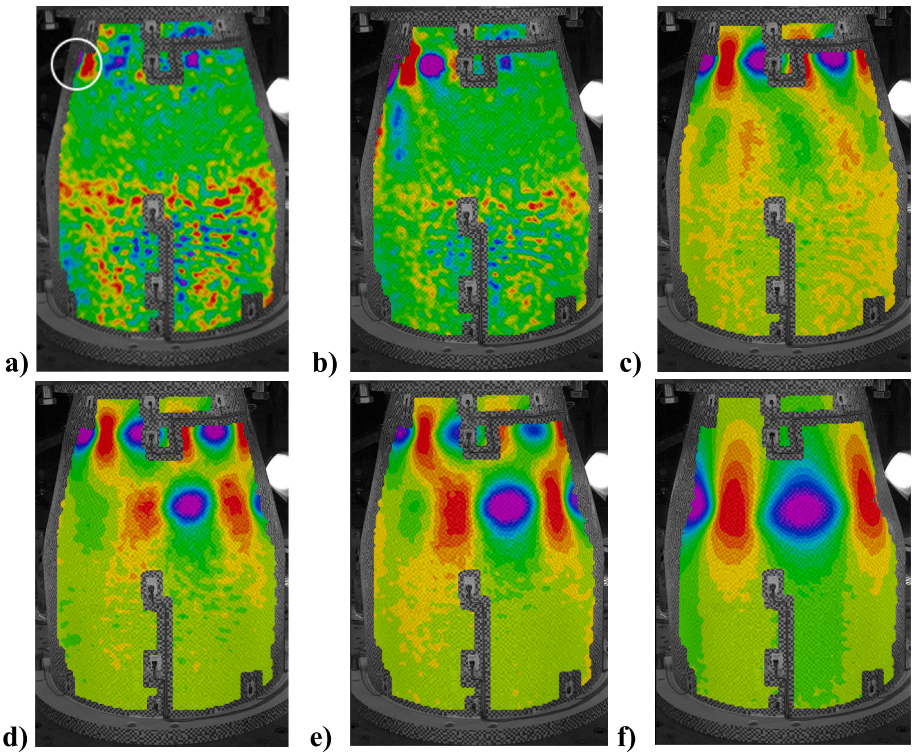


**Fig. 12.** Radial displacement after buckling initiation from high-speed cameras at 180 degrees beginning at a) first image; b) 0.5 ms after (a); c) 2.0 ms after (a); d) 5.5 ms after (a); e) 6.5 ms after (a); f) last image.

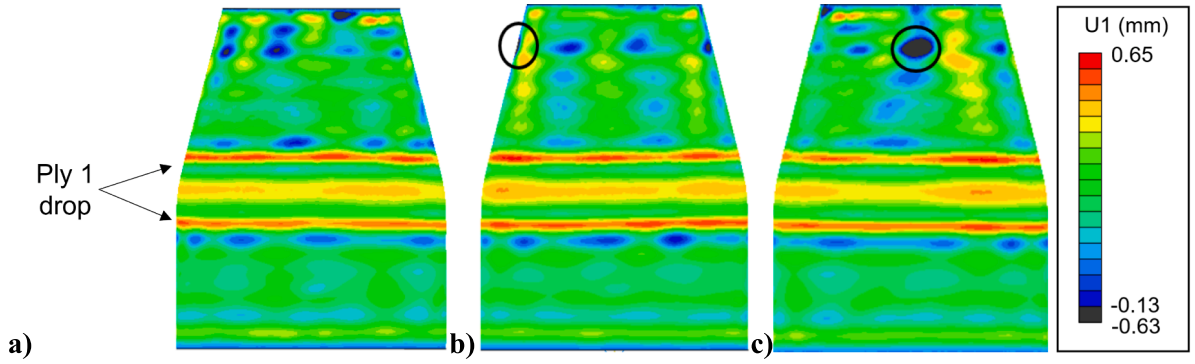


**Fig. 13.** Predicted radial displacements (U1) from Re3CHELL FEM: (a) centered at 0 degrees; (b) centered at 180 degrees; (c) centered at 90 degrees.

difference between measured and predicted axial membrane strains at incipient buckling of −1380 με and −1426 με, respectively, at the cylinder midheight gages. There was 6 % difference between the between measured and predicted axial membrane strains at incipient buckling of −1739 με and −1847 με, respectively, at the transition strain gage. The slopes of the predicted and measured data are in good agreement.

The predicted and measured maximum principal strain contour plots at incipient buckling are shown in Figs. 19 and 20, respectively, and the highest principal strain occurs near the transition region where the hoop strain was greatest as shown by the green-yellow band. The maximum measured principal strain was 2215 με in the center of the transition region in the global DIC system, centered about 180 degrees (Fig. 20b). The predicted strain in the same corresponding region was 2652 με, which was 20 % greater (Fig. 19b). The predicted maximum principal strain was located in the area of the ± 45-degree tow overlap termination at the base of the cone and where the reinforcement ply 2 was dropped. The abrupt changes in the thickness results in a stiffness discontinuity similar to what was observed in the predicted minimum principal strain (Fig. 15). This may have contributed to the large difference between the predicted maximum principal strains and the maximum principal strains measured by DIC.

Better correlation can be observed in Fig. 21 when looking at discrete locations corresponding to the same set of strain gages in Fig. 17. There was a 10 % difference in the hoop membrane strain from the analysis and test incipient buckling for both sets of gages at the transition region (SG1), and the cylinder midheight (SG2). There was good agreement in the slopes of the measured and predicted minimum principal strain for the cylinder midheight gages (SG2). On the contrary, the calculated hoop membrane strain curves at the transition region (SG1) for the measure and predicted began to diverge around 75 kN.

Overall, the correlation between test and analysis for 3CHELL using the updated 3CHELL FEM and Re3CHELL creates confidence in the ability to predict the buckling behavior of composite conical-cylindrical shells. This provides an additional data point for further developing a buckling design methodology for conical-cylindrical shells by demonstrating the ability to predict the buckling behavior for two different

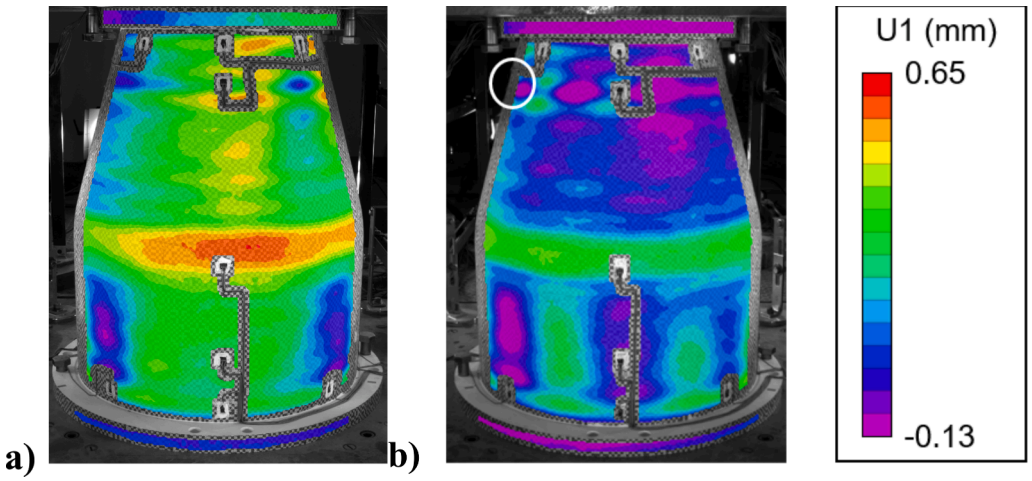


**Fig. 14.** Measured radial displacements (U1) of Re3CHELL: (a) centered at 0 degrees; (b) centered at 180 degrees.

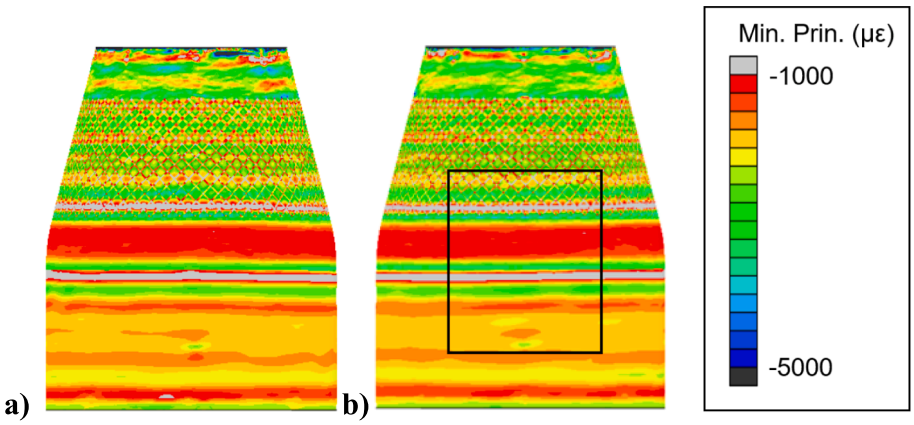


**Fig. 15.** Predicted minimum principal strains from Re3CHELL FEM: (a) centered at 0 degrees; (b) centered at 180 degrees.

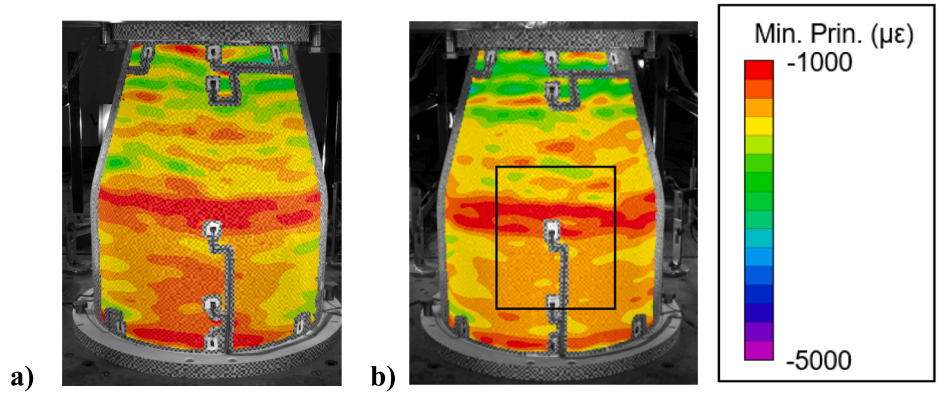


**Fig. 16.** Measured minimum principal strains from Re3CHELL: (a) centered at 0 degrees; (b) centered at 180 degrees.

designs.

### 5.3. 3CHELL versus Re3CHELL

The testing of 3CHELL and Re3CHELL provided valuable information on the buckling behavior for composite conical-cylindrical shells to help establish design guidelines, but it also validates observations on the buckling behavior of conical-cylindrical shells made from a previous study [11]. Specifically, conical-cylindrical shells without reinforcement in the transition region are more inclined to have a reduction in buckling load by including the effects of large displacements and rotations, i.e., geometric nonlinearity, but they are less sensitive to radial imperfections. The opposite is true for conical-cylindrical shells with reinforcement in the transition region, where the increased stiffness of the transition region prevents large displacements and rotations from occurring and the geometrically nonlinear buckling load is close to the linear eigenvalue buckling load. As a result, the shells with transition-region reinforcement are more sensitive to geometric imperfections

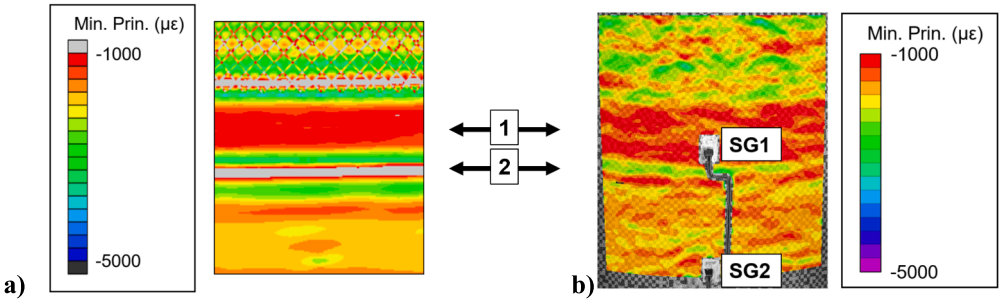


**Fig. 17.** Minimum principal strains from (a) Re3CHELL FEM, and (b) measured from local low-speed DIC system at 180 degrees.

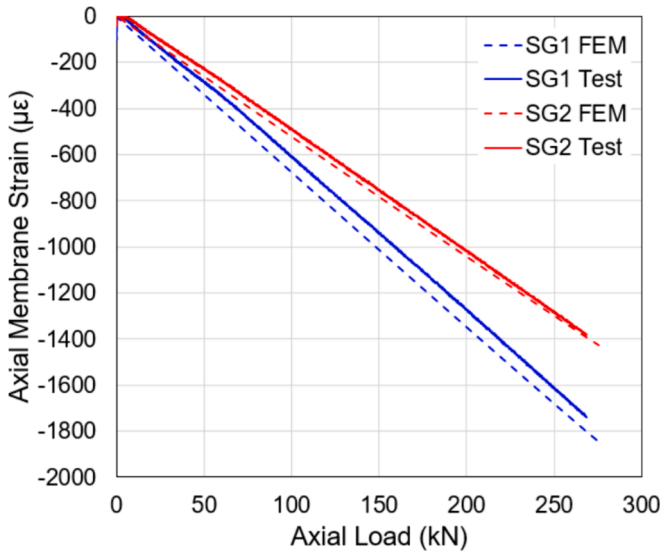


**Fig. 18.** Calculated axial membrane strain from the test and FEM for the midheight cylindrical strain gages (SG1) and the transition strain gages (SG2) at 180 degrees.

than those without reinforcement. To that end, the anticipated gains in the buckling load by adding reinforcement with the intent to increase buckling performance may not be achievable due to the increase in imperfection sensitivity.

The effect of adding reinforcement to the transition region can also be observed when comparing the average axial membrane strain along the length of 3CHELL and Re3CHELL (Fig. 22). The axial membrane strains were calculated by averaging the OML and IML gages. The axial membrane strains at each strain gage axial location were averaged and plotted for 3CHELL (black) and Re3CHELL (red). For this plot, positive axial membrane strains correspond to compressive strains. As can be seen in Fig. 22, the axial membrane strains in the cylindrical regions for 3CHELL and Re3CHELL were similar. The variation in the axial membrane strain in the cylindrical region was within 100 με. It is interesting to note that 3CHELL buckled in the cylinder region, and the axial membrane strains in the cylinder were lower than the conical region strains. For comparison, in 3CHELL the average axial membrane strain in the conical region at the 650 mm was 50 % higher than the axial membrane strains in the cylindrical region at the axial height of 137 mm. Adding reinforcement resulted in lower axial membrane strains in the conical region of Re3CHELL and buckling occurred in the conical region. The average axial membrane strain in the conical region at the axial position of 650 mm, is within 300 με (or 15 %) of the cylindrical axial membrane strain at 137 mm.

The observation that adding reinforcement to the transition region may not increase the buckling load a significant amount can be verified when comparing the mass to the experimental load for Re3CHELL and 3CHELL. The tested Re3CHELL buckling load was 6.2 % higher than 3CHELL tested buckling load, 268.7 kN and 251.8 kN, respectively. The reinforcement added to create Re3CHELL increased the total mass by 5 % of the test article as compared to 3CHELL. A structural efficiency of the test articles can be calculated by dividing the tested buckling load by the mass. Based on the experimental buckling load, the structural efficiency was 74.1 kN/kg for 3CHELL and 75.3 kN/kg for Re3CHELL. Therefore, adding the reinforcement resulted in only a minor increase in efficiency of 1.4 %. According to the buckling loads from the geometrically nonlinear analyses without radial imperfections, it was predicted

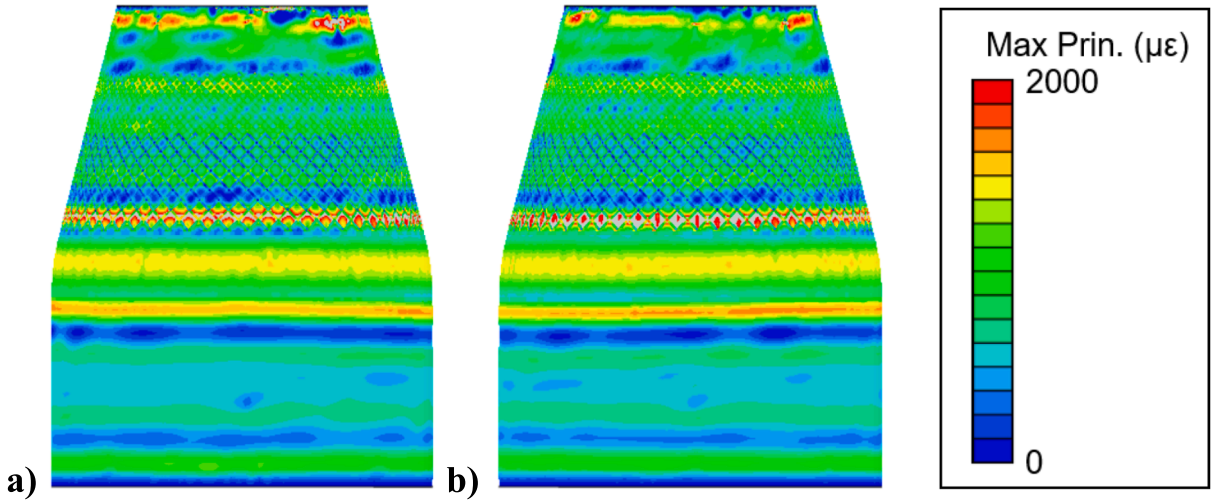


**Fig. 19.** Predicted maximum principal strains from Re3CHELL FEM: (a) centered at 0 degrees; (b) centered at 180 degrees.

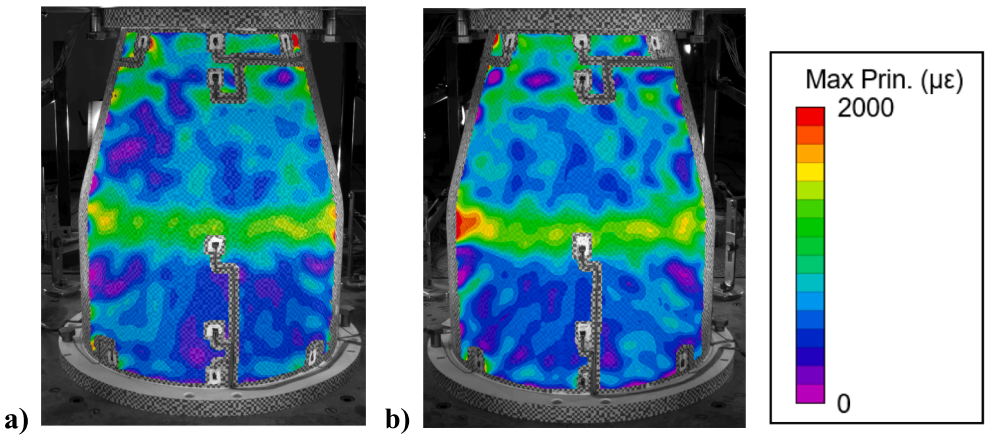


**Fig. 20.** Measured maximum principal strains from Re3CHELL: (a) centered at 0-degrees; (b) centered at 180-degrees.

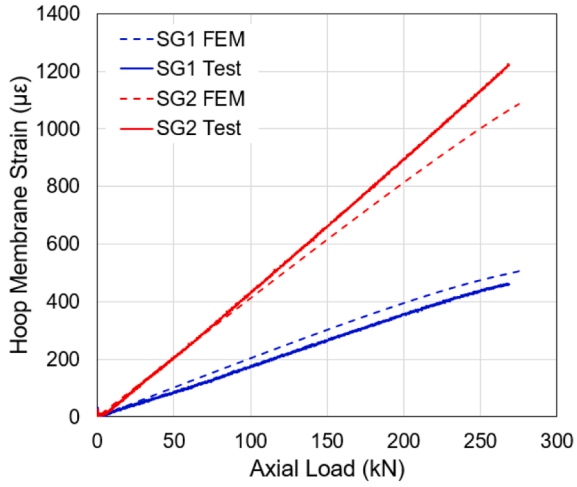


**Fig. 21.** Calculated hoop membrane strain from the test and FEM for the midheight cylindrical (SG1) gages and the transition gages (SG2) at 180 degrees.

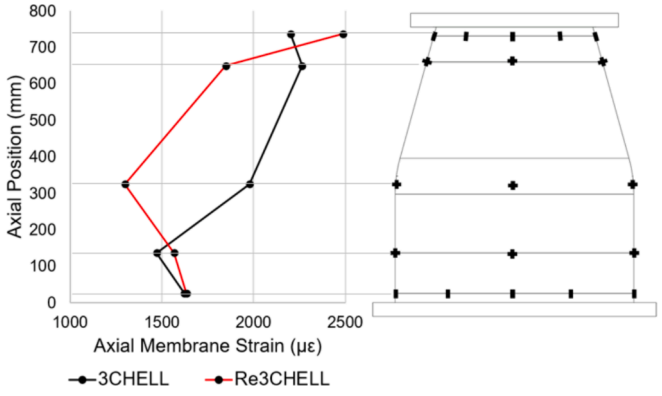


**Fig. 22.** Average axial membrane strains for 3CHELL and Re3CHELL and 240 kN.

that by adding reinforcement to 3CHELL to make Re3CHELL the buckling load with increase from 261.3 kN to 304.5 kN, respectively. Based on these values, it would seem that an 11 % increase in load per unit mass could be achieved when radial imperfections were not included. According to the test data, the added reinforcements only provided an increase of 1.4 % because of the increase in imperfection sensitivity. The experimental results demonstrate that it may not be beneficial to add reinforcement to conical-cylindrical shells to increase the buckling load.

## 6. Concluding remarks

Conical-cylindrical shells have been used in the aerospace industry as launch vehicle stage adapters and payload adapters and can be susceptible to buckling. Though conical-cylindrical shells are being used in practice, there is little buckling design guidance publicly available. To develop buckling design guidance for conical-cylindrical shells, the ability to accurately predict the buckling behavior of composite conical-cylindrical shells must be demonstrated. The successful test and analysis correlation of a composite conical cylindrical shell with and without reinforcement was presented in this paper. Additionally, previous analysis-based observations that adding reinforcement to the cylinder-to-cone transition region may not significantly increase buckling load-to-mass ratio was validated with experimental testing, and therefore care should be taken when adding reinforcement with the intent of increasing the buckling load.

**Funding sources**

This testing was funded by NASA Marshall Space Flight Center Technical Excellence Fund.

## CRediT authorship contribution statement

**Michelle Tillotson Rudd:** Writing – original draft, Visualization, Project administration, Methodology, Investigation, Formal analysis. **Marc R. Schultz:** Writing – review & editing, Supervision, Methodology, Conceptualization. **Nathaniel W. Gardner:** Investigation, Visualization, Writing – review & editing. **Cyrus J.R. Kosztowny:** Resources, Writing – review & editing. **Chiara Bisagni:** Writing – review & editing, Supervision, Methodology, Conceptualization.

## Declaration of competing interest

The authors declare that they have no known competing financial interests or personal relationships that could have appeared to influence the work reported in this paper.

## Data availability

Data will be made available on request.

## Acknowledgments

The work described in this report was conducted in part with support of the NASA Engineering and Safety Center (NESC), in collaboration

with the Delft University of Technology. The authors thank the engineers and technicians in the MSFC Composite Technology Lab and the MSFC Structural Test Lab.

## References

[1] National Aeronautics and Space Administration. Universal Stage Adapter. https://www1.grc.nasa.gov/space/usa/, last accessed on February 2024.
[2] European Space Agency, Deploying Multiple Satellites with Syla and Vespa, https://www.esa.int/Enabling_Support/Space_Transportation/Deploying_multiple_satellites_with_Sylda_and_Vespa, last accessed on May 2024.
[3] Hilburger MW. Buckling of cylindrical shells, NASA Space Vehicle Design Criteria (Structures). NASA SP-8007 2020.
[4] Weingarten VI, Seide P. Buckling of thin-walled truncated cones. NASA space vehicle design criteria (structures). NASA SP-8019 1968.
[5] Bisagni C, Cordisco P. Post-buckling and collapse experiments of stiffened composite cylindrical shells subjected to axial loading and torque. Compos Struct 2006;73(2):138–49. https://doi.org/10.1016/j.compstruct.2005.11.055.
[6] Ning X, Pellegrino S. Imperfection-insensitive axially loaded cylindrical shells. Int J Solids Struct 2015;62:39–51. https://doi.org/10.1016/j.ijsolstr.2014.12.030.
[7] Ning X, Pellegrino S. Experiments on imperfections insensitive axially loaded cylindrical shells. Int J Solids Struct 2017;115–116:73–86. https://doi.org/10.1016/j.ijsolstr.2017.02.028.
[8] Lincoln RL, Weaver PM, Pirrera A, Groh RMJ. Imperfection-insensitive continuous tow-sheared cylinders. Compos Struct 2021;260:112445. https://doi.org/10.1016/j.compstruct.2020.113445.
[9] Wagner HNR, Köke H, Dähne S, Niemann S, Hühne C, Khakimova R. Decision tree-based machine learning to optimize the laminate stacking of composite cylinders for maximum buckling load and minimum imperfection sensitivity. Compos Struct 2019;220:45–63. https://doi.org/10.1016/j.compstruct.2019.02.103.
[10] Rudd MT, Schultz MR, Bisagni C, Buckling behavior of conical- cylindrical shells and design considerations for launch-vehicle structures, AIAA Scitech Forum 2024, AIAA Paper 2024-0034. Doi: 10.2514/6.2024-0034.
[11] Rudd MT, Schultz MR, Gardner NW, Kosztowny CJR, Bisagni C. Analysis and testing of a launch-vehicle-like composite conical-cylindrical shell. AIAA J 2024. https://doi.org/10.2514/1.J063617.
[12] Noevere AT, Collier CS, Mapping AFP Manufacturing Data from VCP to hypersizer for stress analysis and optimization, AIAA Scitech Forum 2018, AIAA Paper 2018-0228. Doi: 10.2514/6.2018-022.
[13] Noevere AT, Collier CS, Harik R, Halbritter J, Development of a Design for Manufacturing Tool for Automated Fiber Placement Structures, AIAA Scitech Forum2019, AIAA Paper 2019-0520, AIAA Scitech Forum 2019. Doi: 10.2514/6.2019-0520.
[14] Patel BP, Nath Y, Shukla KK. Nonlinear thermo-elastic buckling characteristics of cross-ply laminated joined conical- cylindrical shells. Int J Solids Struct 2006;43:4810–29. https://doi.org/10.1016/j.ijsolstr.2005.07.025.
[15] Singh S, Patel BP, Nath Y. Postbuckling behavior of angle-ply laminated joined circular conical-cylindrical shells. AIAA J 2007;45:942–9. https://doi.org/10.2514/1.28358.
[16] Chronopoulos D, Ichchou M, Troclet B, Bareille O. Predicting the broadband response of layered cone-cylinder-cone shell. Compos Struct 2014;107:149–59. https://doi.org/10.1016/j.compstruct.2013.07.055.
[17] Clarkson E, Hexcel 8552 IM7 Unidirectional Prepreg 190 gsm & 35%RC Qualification Statistical Analysis Report, Technical Report NCP-RP-2009-028 Rev B; 2019.
[18] Metallic Materials Properties Development and Standardization (MMPDS), vol. 10, April 2015.
[19] Micor Micorox® Standard Grout Data Sheet, https://www.micorco.com/wp-content/uploads/2014/03/Micorox-Standard-Grout-PDF-3-2014.pdf, last accessed May 2024.
[20] Toray Composite Materials of America, 3960 Prepreg System Data Sheet, https://www.toraycma.com/wp-content/uploads/3960-Prepreg-System.pdf, accessed Febrary 2024.
[21] Solvay, Technical Data Sheet FM 209-1 Film Adhesive; 2018.
[22] Clarkson E, Hexcel 8552S AS4 Plain Weave Fabric Qualification Statistical Analysis Report, Technical Report NCP-RP-2010-011 Rev B. 2012.
[23] Clarkson E, Cytec Cycom 5320-1 T650 3k-PW Fabric Material Allowable Statistical Analysis Report, Technical Report NCP-RP-2012-023 NC; 2015.
[24] Clarkson E, Solvay (Formerly ACG) MTM45-1/CF0525-36%RW 3K PW AS4 Fabric Qualification Statistical Analysis Report, Technical Report NCP-RP-2009-037 N/C; 2019.
[25] ABAQUS/Standard User's Manual. Version 2021 ABAQUS. Inc. USA; 2021.
[26] Vericut Composite Programming, Software Package, Ver. 9.3, CGTech, Irvine, CA, 2023.